IEEE Transactions of Ultrasonics, Sonics and Frequency Control Vol. 50, No. 9, (2003), pp. 1147-1160.

Modeling and Computer Simulation of Ultrasonic/Sonic Driller/Corer (USDC)

Xiaoqi Bao, Yoseph Bar-Cohen, Zensheu Chang, Benjamin P. Dolgin, Stewart Sherrit, *Member*, *IEEE*, Dharmendra S. Pal, Shu Du, and Thomas Peterson

***Abstract*—Simulation and Analytical models for the ultrasonic/sonic drill/corer (USDC) are described in this paper. The USDC was developed as a tool for in-situ rock sampling and analysis in support of the NASA planetary exploration program. The USDC uses a novel drive mechanism, which transfers ultrasonic vibrations of a piezoelectric actuator into larger oscillations of a free-flying mass (free-mass). The free-mass impact on the drill bit creates a stress pulse at the drill tip/rock interface causing fracture in the rock. The main parts of the device (transducer, free-mass, bit, and rock) and the interactions between them were analyzed and numerically modeled to explore the drive mechanism. Each of these interactions is normally described by a time-dependent 2 or 3 dimensional model involving slowly converging solutions, which makes the conventional approach unsuitable for USDC optimization studies. A simplified integrated model using tabulated data was developed to simulate the operation of the USDC on desktop PC and successfully predicted the characteristics of the device under a variety of conditions. The simulated results of the model and the experimental data used to verify the model are presented.**

***Index Terms*- piezoelectric actuators, ultrasonic sonic drill simulation, free-mass resonance, impact modeling, rock coring.**

I. Introduction

FUTURE NASA exploration missions to Mars, Europa, Titan, or possibly comets or asteroids are seeking to perform sampling, in-situ analysis and perhaps the return of material to Earth for further tests. Existing drilling techniques are limited by the need for large axial forces and holding torques, high power consumption and an inability to efficiently duty cycle. Lightweight robots and rovers have difficulties accommodating these requirements. To address these key challenges to the NASA objective of planetary in-situ rock sampling and analysis, an ultrasonic/sonic driller/corer (USDC) was developed [1], [2]. The actuator of the USDC is an ultrasonic horn transducer that is driven by a piezoelectric stack. Unlike the typical ultrasonic drill where the drill stem is acoustically coupled to the transducer, the horn transducer in the USDC drives a free flying mass (free-mass), which bounces between the horn tip and a drill stem at sonic frequencies. The impacts of the free-mass create stress pulses that propagate to the interface of the stem tip and the rock. The rock fractures when its ultimate strain is exceeded at the rock/bit interface. This novel drilling mechanism has been shown to be more efficient and versatile than conventional ultrasonic drills under a variety of conditions. The low mass of a USDC device and the ability to operate with minimum axial load with near zero holding torque (see Fig. 1) offers an important tool for sample acquisition and in-situ analysis. Another important characteristic of the USDC is the capability to operate in the challenging environment of space.

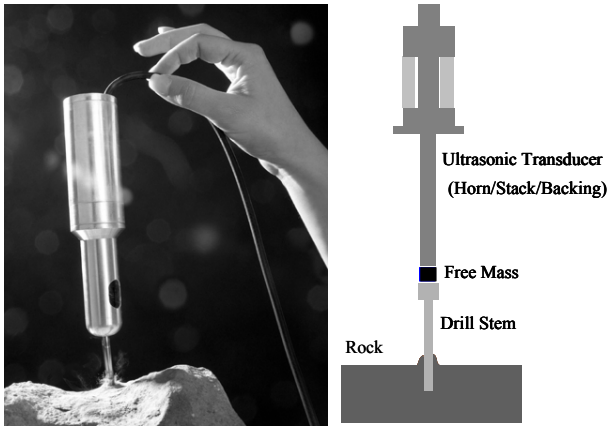

Fig. 1. The USDC is shown coring with minimum axial force and holding torque (left), and a schematic diagram of the USDC device (right).

The model developed for the USDC describes five elements involved in the drilling i.e. the electrical driver, ultrasonic transducer, free-mass, drill stem, and the rock. In the initial modeling the main elements and the interaction between them were analyzed and modeled separately. A one-dimensional model was then developed for each interaction and an integrated software program was developed to simulate the operation of all parts of the USDC. The strain that is induced in the rock was calculated and the drilling rate was estimated based on the specific energy required to fracture the rock. This paper reports on the individual models and the algorithms of the integrated program. The computed results and the comparison with the experimental tests are also presented.

II. Modeling

The USDC device consists of three main parts: an ultrasonic transducer (piezoelectric stack, a backing element, and a horn), free-mass and a drill stem. The ultrasonic transducer vibrates at a frequency of about 20kHz. These vibrations of the horn tip excite the free-mass, causing it to hop between the horn tip and the top of the drill stem with average frequencies in range of 100 to

This work was supported by The Mars Exploration Technologies under a contract with the National Aeronautics Space Agency (NASA) funded the research at the Jet Propulsion Laboratory (JPL), a division of the California Institute of Technology.

Xiaoqi Bao, Yoseph Bar-Cohen, Zensheu Chang, Benjamin P. Dolgin, and Stewart Sherrit, are with the Jet Propulsion Lab, Pasadena, CA 91109 USA (telephone: 818-354-0298, e-mail: xbao@ jpl.nasa.gov). Dharmendra S. Pal, Shu Du and Thomas Peterson are with Cybersonics Inc., 5368 Kuhl Rd., Erie, PA 16510 USA.

1000 Hz. The free-mass transfers energy from the ultrasonic transducer to the drill stem. The shock waves caused by the impacts of the free-mass propagate to the bit/rock interface and wherever the rock is strained past its ultimate strain it fractures. In order to determine the critical issues related to the control and optimization of the drill models the interaction at the various interfaces of the drill were investigated. The four interactions that were modeled include: 1) transducer with the driving circuit, 2) horn tip with the free-mass, 3) free-mass with the drill stem and 4) base of the drill stem (bit) with the rock. In order to integrate these models into a computer program to simulate the operation of the USDC, efforts were made to simplify the models and reduce the computing time.

A. Ultrasonic horn transducer

The horn transducer consists of a steel-backing block, a PZT-8 stack, a steel horn and a pre-stress bolt as shown in Fig. 2. The overall dimensions of the elements of the transducer are shown in Table 1.

Table 1. The dimensions of the elements of the transducer

Piezoelectric Stack
OD.=0.025 m ID. = 0.0125 m L= 0.0212 m n=4
Stress Bolt
Screw: D.=0.00952 m L= 0.0339 m Head: D.=0.011 m L= 0.00902 m
Backing
D.=0.0268 m L= 0.0127 m
Horn
Base: D.=0.0268/0.0366 m Tip: D=0.0089 m L= 0.0683 m

The transducer is a composite longitudinal vibrator with varying cross sections and can be modeled by the Mason equivalent circuit as presented in a previous paper [3]. In order to include engineering details in the final transducer design the finite element approach was used to determine the full frequency response of this piezoelectric device. An electromechanically coupled element [4] was applied to model the piezoelectric material, which is available in commercial software ANSYS [5].

In this high power ultrasonic application, the transducer is designed and fabricated to have high mechanical Q, and is operated at or near its first longitudinal resonance frequency. Using modal analysis allowed us to isolate and concentrate on this resonance mode and it simplifies the model and reduces the computing time. Solving the generalized eigenvalue problem of finite element equations, the resonance frequencies and corresponding mode shapes can be found. We obtained a set of resonance frequencies, $\omega_1, \omega_2, \ldots, \omega_n$ and normalized mode shapes (eigenvectors)

$$\{\xi_1\}, \{\xi_2\}, \ldots, \{\xi_n\} \qquad (1)$$

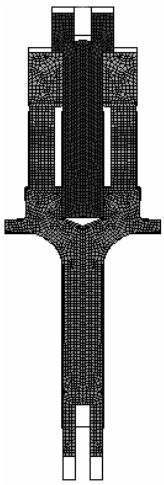

Fig. 2. The calculated modal shape of the horn transducer at a frequency of 22.668 kHz. The meshed areas represent the cross section of the deformed transducer and the outline represents the un-deformed surfaces.

Figure 2 shows the model shape of the first nonzero-frequency resonance of the transducer calculated by ANSYS. The mode is basically a longitudinal vibration with larger displacement at the horn tip than at the surface of the backing. The resonance frequency was found at 22.688 kHz using the material property data provided by the manufacturers, which was found to be very close to the measured frequencies of 22 to 23 kHz

By expressing the displacement as the summation of the mode shapes

$$\{\xi\} = \sum_n d_i \{\xi_i\}, \qquad (2)$$

the finite element equations can be converted to a modal equation and simplified by representing it as an equivalent circuit for convenience in computation as was done in previous work [6].

The modal equation can then be written as

$$\begin{aligned} &(\omega_i^2 + j\omega R_i - \omega^2) d_i = p_i V + Fm_i \\ &Q = \sum_n p_i d_i + C_0 V \end{aligned} \qquad i = 1, \ldots, n \qquad (3)$$

where d_i is the amplitude of the mode i, Q is the electric charge on the electrode, R_i, p_i and Fm_i are effective damping, electromechanical coupling and force for the modes respectively. The R_i and p_i can be calculated from the finite element matrixes, and Fm_i is expressed as

$$Fm_i = \{\xi_i\}^T \{F\}, \qquad (4)$$

where $\{F\}$ is the vector of the force applied on the nodes.

Only the first longitudinal mode is taken into account in the analysis. With these substitutions (3) becomes

$$\begin{aligned}(\omega_1^2 + j\omega R - \omega^2)d &= pV + Fm \\ Q &= pd + C_0 V\end{aligned}, \tag{5}$$

where the subscripts are omitted for simplification.

A further simplification is shown for (5) by representing the response of the device by an equivalent circuit around resonance as is shown in Fig. 3, where the subscripts *m* are added to denote that the symbols actually represent mechanical variables and parameters. The element in the dashed square is the sketch of electric driving circuit.

Upon inspection we have L_m = 1, C_m = $1/\omega_1^2$ and the mechanical "current" I_m is the modal velocity

$$I_m = \dot{d} . \tag{6}$$

When the transducer is driven electrically and is mechanically unconstrained (no impacts with the free-mass), the modal velocity can shown to be

$$I_m = \frac{pV}{j(\omega L_m - \frac{1}{\omega C_m}) + R_m} . \tag{7}$$

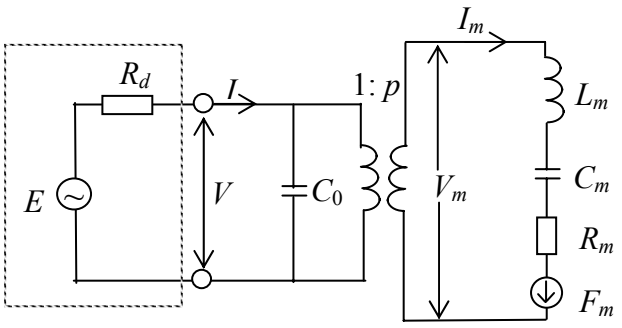

Fig. 3. A schematic diagram of the equivalent circuit of the transducer around resonance. The generator source is shown in the dashed square.

B. Reaction of free-mass impacts to the transducer

During the operation of the USDC, a small preload force, either from gravity or from a spring is applied to the transducer. The force pushes the transducer down toward the free-mass and the bit. A harmonic voltage at a frequency around the resonance drives the transducer. The free-mass is energized by the vibrating horn tip, then, bounces between the bit and horn tip and maintains a gap between them. The impacts of the free-mass on the horn tip affect both vibration and translation movements of the horn transducer.

1) Translation movement of the horn transducer

During operation the preload force is constant and produces an acceleration a of the transducer. If we now suppose an impact happens at time t_I, and contact time is very short, the contact force can be expressed as

$$F_c = f_I \delta(t - t_I) , \tag{8}$$

where δ is the delta function. Using momentum conservation during the impact, we have

$$f_I = -m\Delta v_I , \tag{9}$$

where m and Δv_I is the mass and velocity of the free-mass respectively. Each impact results in a change of the center of mass (COM) velocity of the horn by

$$\Delta U_I = \frac{-m\Delta v_I}{M} H(t - t_I) , \tag{10}$$

where M is the total mass of the horn transducer, and H is the step function. Therefore, the COM velocity of the transducer becomes

$$U = U_0 + at + \sum_I \Delta U_I . \tag{11}$$

The displacement of the transducer can then be determined by calculating the time integral of the velocity.

2) Vibration of the transducer with constant harmonic voltage driving

When the source resistance R_d as shown in Fig. 3 is zero, the transducer is driven by a constant voltage. In this case, the vibration of the transducer can be solved explicitly. From the equivalent circuit, we can write the corresponding differential equation as

$$L_m \ddot{d} + R_m \dot{d} + C_m d = pV + F_m . \tag{12}$$

The solution of this equation is the summation of the vibration induced by the electric voltage V and the vibration caused by the mechanical force F_m. The steady solution for a harmonic voltage $V = V_0 \exp(j\omega t)$ is

$$I_{me} = \dot{d}_e = \frac{pV}{j(\omega L_m - 1/\omega C_m) + R_m} . \tag{13}$$

A mechanical force is created by the impacts of the free-mass on the horn tip and can be determined from (4), (8) and (9), to be

$$F_m = \xi_t f\delta(t-t_I) = -m\Delta v_I \xi_t \delta(t-t_I), \quad (14)$$

where ξ_t is the tip displacement of the mode shape. The solution of (12) for the impact force F_m is a free ring-down vibration after the impact time t_I and is expressed as

$$I_{mI} = \dot{d}_I = -\frac{m\Delta v_I \xi_t}{L_m}\exp[(-\alpha + j\omega_f)(t-t_I)], \quad t > t_I, \quad (15)$$

where α is damping coefficient and ω_f is the free vibration frequency, and

$$\alpha = -\frac{R_m}{2L_m} \quad (16)$$

$$\omega_f = \sqrt{\omega_1^2 - (R_m/2L_m)^2}\,. \quad (17)$$

The final solution of the model velocity is

$$I_m = \dot{d} = \dot{d}_e + \sum_I \dot{d}_I = I_{me} + \sum_I I_{mI}\,. \quad (18)$$

3) Transducer driven by a driver with output resistance

In General, the output resistance of electronic drivers is not zero. The resistance will reduce the output voltage, increase energy loss and change the characteristics of the vibrations induced by the impacts.

The same approach utilized in the previous section can be applied to the case of non-zero output impedances of the drive circuit which results in a slightly more complicated solution. The steady solution of the electric driving voltage in this case is then

$$I_{me} = \dot{d}_e = \frac{pEZ_x/(R_d + Z_x)}{j(\omega L_m - 1/\omega C_m) + R_m}, \quad (19)$$

where the impedance of the transducer Z_x is

$$Z_x = \frac{j(\omega L_m - 1/\omega C_m) + R_m}{j\omega C_0[j(\omega L_m - 1/\omega C_m) + R_m] + 1/p^2}\,. \quad (20)$$

The solution for the impact is

$$I_{mI} = \dot{d}_I = -\frac{m\Delta v \xi_t}{L_m}\exp[S(t-t_I)], \quad (21)$$

where S is the solution of the following polynomial equation

$$\begin{aligned} L_m C_m R_d C_0 S^3 + (L_m C_m + R_m C_m R_d C_0)S^2 \\ + (R_m C_m + p^2 R_d C_m + R_d C_0)S + 1 = 0 \end{aligned}\,. \quad (22)$$

This cubic equation has one real root and a pair of conjugate complex roots. For the free attenuating vibration, the solution *S* is in the form as

$$S = -\alpha + j\omega_f\,. \quad (23)$$

Although it is possible to obtain explicit expression of the solution, the expression is cumbersome and not accurate in practical numerical calculations. We have chosen to solve the equation by following steps:

1. Find the real root numerically.
2. Factor the equation and reduce it to square equation.
3. Solve the square equation.

The results for the transducer with typical parameters are shown in the Fiq.4. As expected, when the output resistance of the driver increases from 0 to infinity, the free vibration frequency varies from resonance frequency of the transducer to anti-resonance. The resistance increases the damping and decreases the Q value of the oscillation. The effect reaches the maximum around $\omega_f R_d C_0 = 1$.

Fig. 4. The effect of output resistance of driver on the free vibration of the horn transducer and the effective Q are shown.

C. Interaction between transducer and the electric driver

Power output from the voltage source E is the time averaged integral of product of multiplication of the source voltage by the current and is expressed as

$$\begin{aligned} P_E &= \frac{1}{T}\int_T E(t)I(t)dt \\ &= \frac{1}{T}\int_T E(t)I_e(t)dt + \frac{1}{T}\int_T E(t)\sum_I I_I(t)dt \end{aligned} \quad (24)$$

or

$$P_E = P_{Ee} + P_{EI}\,, \quad (25)$$

where the first item in (24), P_{Ee}, is the power with no free-mass loading and P_{EI} is the power change introduced by the free-mass loading. $I_e(t)$ is the current though the

source due to the electric drive voltage, and $I_I(t)$ is the current due to the free-mass impacts,

$$I_e(t) = \mathrm{Re}\left(\frac{E}{Z_x(\omega) + R_d}\right) \tag{26}$$

$$I_I(t) = \mathrm{Re}\left(\frac{pI_{mI}}{j\omega_f C_0 R_d + 1}\right). \tag{27}$$

The power lost on the resistor R_d is calculated using the time-averaged power

$$P_d = \frac{1}{T}\int_T R_d[I(t)]^2 dt = \frac{R_d}{T}\int_T [I_e(t) + \sum_I I_I(t)]^2 dt \,. \tag{28}$$

It should be noted that, in these power calculations, all voltages and currents are expressed as real functions of time rather than their complex expression. Beside, the currents introduced by the impacts $I_I(t)$ attenuate with time and oscillate at the frequency ω_f, which may be different from the driving frequency ω. Therefore, the integrals in (24) and (28) are in a general form of

$$Int = \int \cos(at + f)\cos(bt + g)e^{-ct} dt \,, \tag{29}$$

which can be calculated explicitly.

D. Free-mass driven by the horn transducer

1) Simple collision model

A simple collision model was applied first to explore the basic mechanism of the horn/free-mass interaction. In this model, we assume that the energy loss and time duration of the impact is negligible, and the mass of the horn is much larger than the free-mass. Using the conservation of momentum and energy, we have

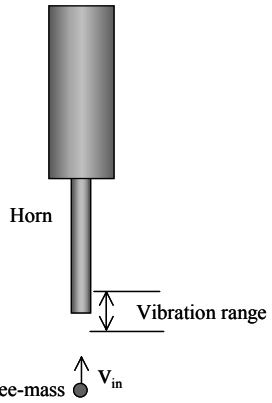

Fig. 5. A Schematic of the horn driving the free-mass.

$$v_{out} = v_{in} + 2v_t \,, \tag{30}$$

where v_{in} is the incoming velocity of free-mass prior to impact with the horn as shown in Fig. 5, v_{out} is the outgoing velocity after impact with the horn, and v_t is the velocity of the horn tip.

The horn vibrates at the resonance frequency. The tip displacement is harmonic and is represented by

$$u = u_0 \cos(\omega t + \vartheta) \,, \tag{31}$$

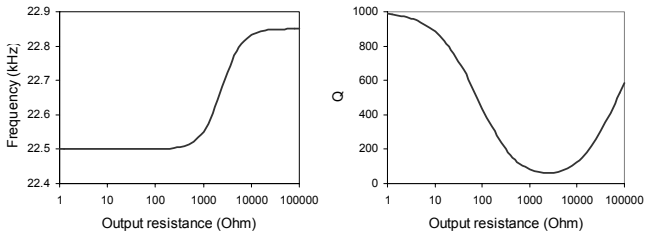

where time zero is set at the moment when the free-mass just reaches the edge of the range of tip vibration. The velocity of the horn tip is found by taking the time derivative of the displacement and can be written as

$$v_t = -\omega u_0 \sin(\omega t + \vartheta) \,. \tag{32}$$

A computer model, which traces the position of the free-mass until it leaves the tip vibration range ($2u_0$), was programmed. The routine calculates the free-mass speed after each interaction with the horn. The outgoing speeds of the free-mass versus the vibration phase are shown in the Fig. 6 for different ratios of incoming speed/tip velocity amplitudes. The model accounts for multiple impacts that may become possible when the impact is timed appropriately, which are shown in Fig. 6b and 6c at a phase of 50°.

Although (30) implies that the v_{out} may be less than v_{in} when the tip velocity v_t is negative, the computed results show that the free-mass velocity does increase on average after interaction with the vibrating tip. Fig. 7 shows the average rate of the free-mass energy increase after impacts assuming a uniform probability of the relative phase in the range of 0° – 360°. The increased rate is higher the lower the relative incoming speed. The causes of the increase are

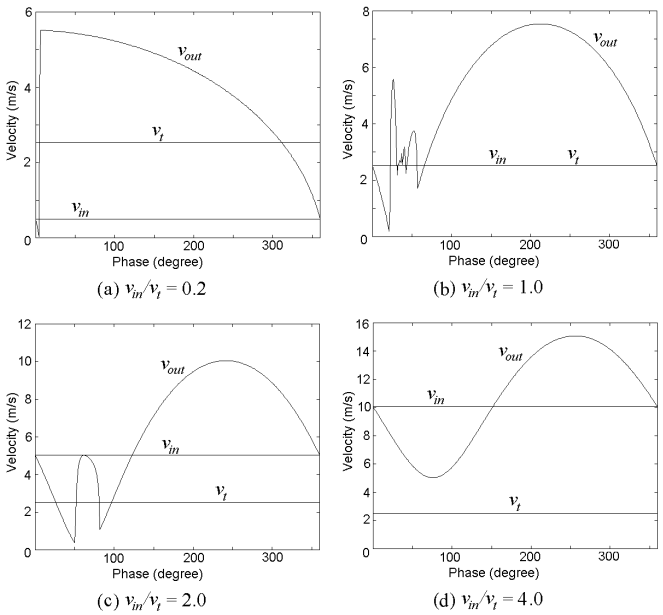

Fig. 6. The speeds of the free-mass after impacts, v_{0ut}, versus relative tip vibration phase for different incoming speeds v_{in}. The solid horizontal lines indicate the levels of the incoming speed v_{in} and the amplitude of tip velocity v_t.

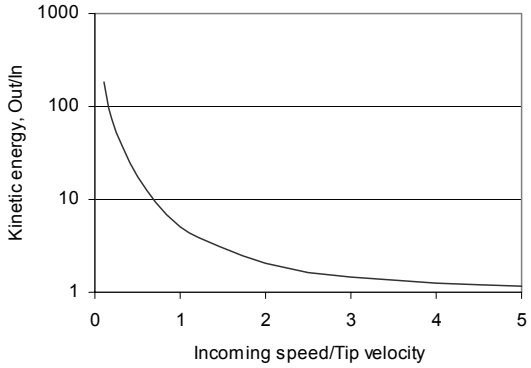

Fig. 7. The curve shows the average increase of the free-mass kinetic energy after interaction as a function of the relative initial free-mass speed predicted by simple collision model.

(1) Although the tip velocity alternates harmonically and is negative half of the time, the free-mass has less chance to interact with the tip when the tip is pulling back, especially if the free-mass speed is low. This results in the phase range where $v_{out} > v_{in}$ always being greater than half the full range as shown in Fig.6.

(2) If the first impact results in low or negative v_{out}, the free-mass will stay in the tip vibration range longer and has the possibility to be hit a second time. The irregularities of the curves around a phase of 50° in Fig. 6b and 6c are due to the multiple impacts between the free-mass and the tip.

2) Finite element model

In the simple collision model, we assumed that the horn mass is much greater than the free-mass. This is true if we include the total mass of the horn transducer. However, in the short time duration that the impact lasts, the impact wave propagates to a limited range within the horn transducer. The remaining part of the transducer is actually not involved in the impact. So, the assumption of a horn mass much greater than the free-mass may not be correct. To explore the details of the real impact/driving process, a finite element model was developed.

In the model, the horn transducer is truncated to a λ/4 long bar. A symmetric boundary condition is applied at the other end of the bar. The validity of this truncation is based on the fact that the any structure difference in the area far from the point of impact will not make a difference to the free-mass bouncing process. From the view of wave propagation the free-mass should not "feel" the structure difference in the area, as long as the free-mass leaves the tip surface before the impact wave can propagate through the medium and be reflected back to the impact spot. Axisymmetrical solid elements are used to represent the horn tip. The initial conditions, i.e. the displacements and velocities of the nodes, are set to typical longitudinal vibration values in the bar. Compression only link elements are placed between the nodes on the surfaces of the free-mass and the horn tip in the contact area. The free-mass is treated as a rigid block with a curvature in the contact area.

The finite element approach provides a more accurate description of the free-mass speed after the collision and the time duration of the collision (see Fig. 8). Comparing with the simple collision model (see Fig. 9), ones can see that the maximum speed is typically lower compared to the simple collision model. This implies a limited effective mass of the horn. The curve also displays a phase shift that can be explained by considering the contact time.

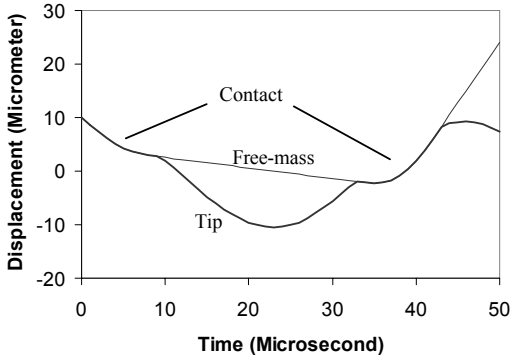

Fig. 8. The curve shows the free-mass and tip surface displacement as a function of the time in a collision calculated by the finite element method. The horn vibrates at 22.5 kHz with tip amplitude of 10 μm. The free-mass incoming speed is equal to the tip peak velocity of 1.39 m/s.

This figure shows double contacts occur in the interaction.

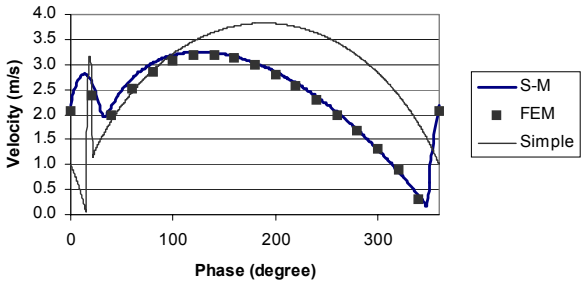

Fig. 9. The velocity of the free-mass as a function of the phase computed by the simple collision, spring-mass and FEM models.

3) Spring-mass model

The finite element approach explored two phenomena that were not accounted for in the simple collision model, elasticity of the horn and the effective mass involved in the impacts. Based on these phenomena, a spring-mass model was developed. The model uses a mass and two springs to represent the horn as shown in Fig. 10.

The parameters of the mass M and front spring k are determined using the rebound velocity and contact time obtained by the finite element approach. The top spring constant K is set by the resonance frequency of the horn transducer. An example of the results of the model is presented in Fig. 9. The results are found to agree exceptionally well with the finite element results. The spring-mass model therefore provides a more time efficient solution with reasonable accuracy, which was required by the integrated simulation program.

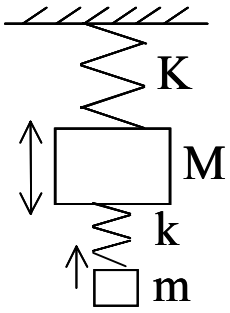

Fig. 10. A sketch of the spring-mass model for horn/free-mass interaction

Figure 11 shows the average kinetic energy change of the free-mass during interaction with the horn versus the parameters of the mass and normalized incoming speeds calculated by the spring-mass model. v_t is the velocity amplitude of the horn tip (1.39 m/s in the calculation). The kinetic energy change decreases when the mass or the incoming speed increases. The effective masses and time delays were used in the final model of the USDC.

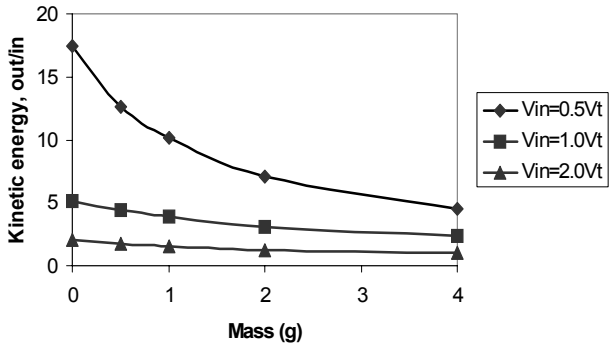

Fig. 11. Average energy of the free-mass after interaction with horn as a function of the mass and incoming speed computed by the spring-mass model. The energy is normalized to the energy before the interaction.

E. Free-mass bouncing from the drill bit

The typical geometry of the drill stem is shown in Fig. 12. It consists of a head and a thin cylindrical bar. The free-mass impacts the head and creates a stress wave that propagates toward the lower end of the bit. A finite element model, which is similar to that used for horn tip and free-mass interaction, was utilized to investigate the impacts. The length of the drill stem was fixed to be long enough to avoid the interference of a reflected wave from the bottom. An example of the results for the displacement of the free-mass and the center of the top surface of drill bit as a function of time is shown in Fig. 12.

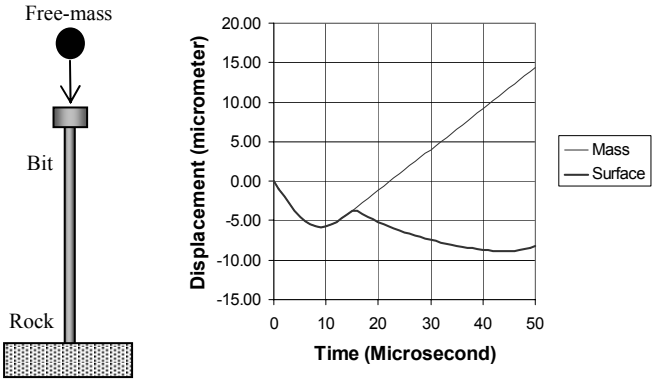

Fig. 12. Finite element displacement results of the free-mass bounce from the drill bit. The free-mass is 2 grams and the incoming speed is 1 m/s. The rebound speed is 0.5 m/s and contact time 15 μs.

The free-mass is 2 grams with speed of 1 m/s. The curvature of free-mass surface at the contact area is 0.1 m. The steel stem is 3 mm in diameter and has a head of

diameter 12 mm and is 6 mm long. The total height of the drill bit is 100 mm. A symmetric boundary condition is applied at the bottom. The rebound speed was found as 0.5 m/s. The ratio of rebound speed to the incoming speed is dependent on the value of the mass as shown in Fig. 13. The affect of the incoming speed is not significant.

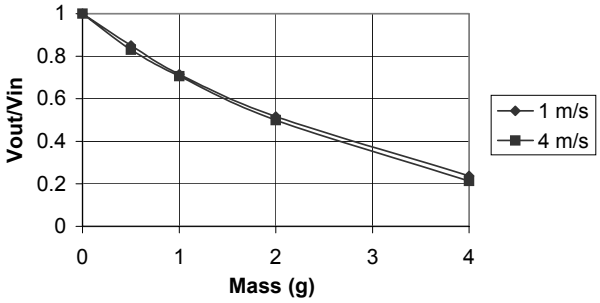

Fig. 13. Bounce speed versus mass and incoming speed computed by FE model

By investigating the stress in the stem, we found that the impact resulted in a compression plane wave propagating with a velocity around 5000 m/s, which is in agreement with the longitudinal wave velocity in thin steel bar. The stress at the bottom of the stem is presented in Fig. 14 as a function of time.

F. Integrated computer simulation model

A computer program was developed to simulate the operation of the drill system including the horn transducer, free-mass, drill stem and the electric driver. The program was able to predict the performance of the USDC under a variety of initial conditions.

In the simulation, we assumed that the vibrations in the drill bit induced by the previous free-mass impacts were attenuated when the free-mass returns and hits the drill stem. We also neglected the movement of the drill stem with respect to the rock, since it is very slow in comparison to the quick motion of the free-mass. Therefore the top surface of the drill stem is set at the same position for the each of the impacts. Experimental observations suggest that this is a valid assumption. Replay of the video record taken by a high-speed camera showed the motion of the upper end of the drill stem was very small comparing with the free-mass or the horn transducer.

The flowchart of the calculation procedure is presented in Fig. 15. We start the simulation by setting the initial values of the position and velocity of the horn and the free-mass. The software traces the translation movements of the horn transducer and the free-mass as well as the vibration of the horn as a function of time. It predicts the time and location of the free-mass/horn or free-mass/bit collision. Using the data of the free-mass/horn and free-mass/bit impacts that were determined from the models mentioned in previous paragraphs, the simulation calculates the changes of the variables as time evolves. The movements and vibration due to the impact are recorded along with the impact momentum and time. The program then proceeds to determine the next impact. The energy supplied by the electric source and delivered to the transducer is integrated and recorded concurrently. The statistics reported by the program include; electric input power, mechanical output power delivered to the drill stem, average and distribution of the free-mass speed, etc. The first 20% of the events are excluded in order to eliminate the possible influence of the initial settings.

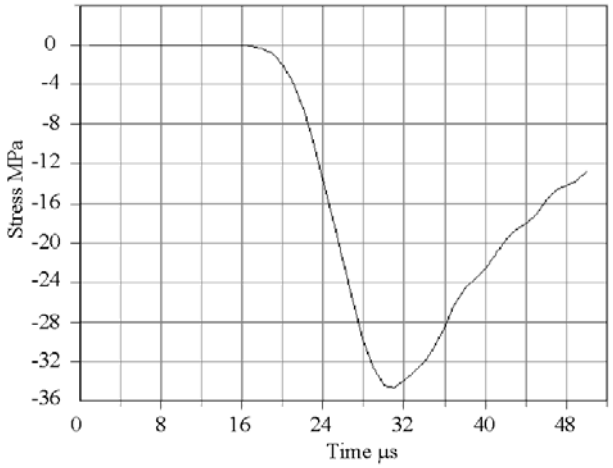

Fig. 14. The stress as a function of times at the bottom of the stem that is 100 mm from the top surface.

Typical simulation results are shown in Fig. 16-19. In this simulation, the transducer is excited by 100 V peak voltage at resonance frequency of 22.5 kHz. The mechanical Q of the transducer is 1000. The free-mass weighs 2 grams, the transducer with the mounting platform weighs 800 grams and Earth gravity[1] is applied as the preload force. In Fig. 16, each dot represents an impact event of the free-mass with the bit stem. The X-axis is the time of each impact and the Y-axis is the velocity of the free-mass before impact, normalized by the horn tip vibration velocity without loading, in this case, 6.67 m/s. The pattern looks like a random sequence of impacts. No repeat cycle has been observed. Actually, no random perturbation is added to the program and the simulation is repeatable for fixed initial conditions. Therefore the simulation actually shows a pseudo-random procedure. The amplitudes of the horn vibration at the moment before horn/free-mass contact are presented in Fig. 17. The amplitudes are normalized to the horn vibration amplitude without loading. As expected, the average amplitude is lower than that without loading because the horn loses energy while driving the free-mass. Fig. 18(a) shows the heights of the horn transducer in the free-mass/horn impact events. Ones can see the trace of the translation movement of the horn transducer. Fig. 18(b) shows an example of experimental data of the horn movement in a drilling test.

[1] The total mass reflects the contribution of the test stand. Later, a lighter test stand reduced the effective 800 grams by a factor of nearly 2.

The data was obtained from images taken by a high-speed camera. The simulation results successfully showed a characteristic of the movement similar to the experimental data. The frequency, height and randomness of the jumps appear to agree very well with the data

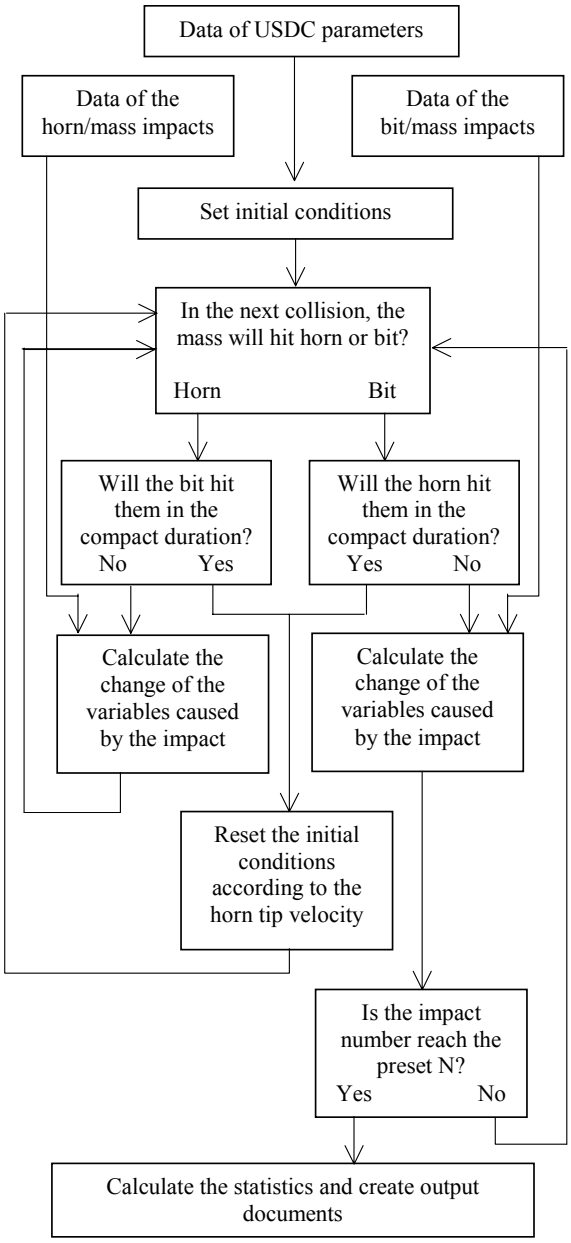

Fig. 15. Flow chart of the simulation program

The average speed of the free-mass hitting the drill stem was found to be 2.4 m/s. Fig. 19 shows the frequency of the impacts within different momentum ranges. This is an alternative presentation of the distribution of impact momentum. This data representation is useful for the estimation of the drilling rates, which will be discussed later.

The electric input power is 21 W and the mechanical power transferred to the drill stem is 6.5 W. The average hit frequency is 1100 Hz. The contact time of each free-mass/bit impact is short, in the range from 10 to 15 μs (see Fig. 12). Therefore, the average mechanical power delivered to the drill bit in the contact time is as high as 540 W.

The results show that, by using the free-mass to convert the high frequency vibrations to low frequency impacts, the low continuous electric input power is converted to a high mechanical power. The later creates large enough strain in the rock to enable efficient drilling.

G. Strain and stress in rocks

In order to better understand the fracture of rocks under impact loading from a drill or a corer, a finite element model was developed using ANSYS. For the purpose of simplifying the problem, the rock is modeled as a circular cylinder with bottom surface fixed and the drill/corer impacts at the center of the top surface. This simplification makes the problem axis-symmetric. By using the axis-symmetric elements available in ANSYS, the original three-dimensional problem is now reduced to a two-dimensions. The element size is made very fine near the drill/corer bit, and becomes coarser and coarser as it goes further away from the bit.

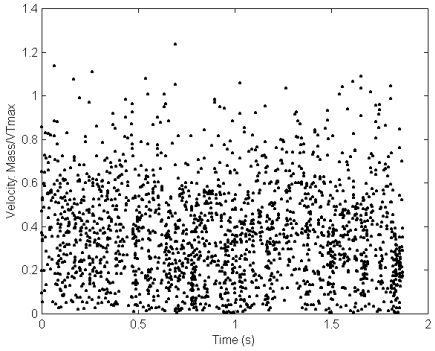

Fig. 16. Free-mass velocity normalized by the horn tip vibration velocity without loading of 6.67 m/s

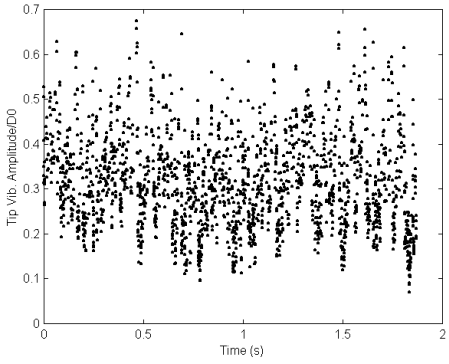

Fig. 17. Horn vibration amplitude normalized by the amplitude without loading

Preliminary results were derived by assuming that the circular cylinder is made of isotropic material with a Young's modulus of 11.2 GPa, poisons ratio of 0.3, and density of 2470 kg/m^3. The impact loading from the drill has a peak value of 50 MPa and duration of 50 μsec, as shown in Fig. 20.

Contour maps of the maximum principal strain were plotted and used as indication of fracture of rocks. It also shows how the elastic waves propagate in the rock. Fig. 21 shows the contour maps of the cylinder for drilling and coring, respectively. The drill bit is 3 mm in diameter. The corer has an inner diameter of 2.4 mm and an outer diameter of 3 mm.

The results show qualitative features of the rocks fracture under ultrasonic/sonic drilling or coring. From Fig. 21 we find that the highest principal strain occurs at the edge of the drill bit. For the corer, the highest principal strain appears at both the outer and inner edge of the corer. It implies that the fracture is likely going to happen at the edge, which is confirmed by viewing the high speed filming during drilling. By comparing the various strain profiles in Fig. 21, we find that the maximum principal strain under coring is higher than that under drilling, and the area of high principal strain under coring is also larger than that under drilling. It implies that with the same outer diameter and under the same loading, a corer drills faster than a solid drill of the same diameter. This is confirmed by experiments.

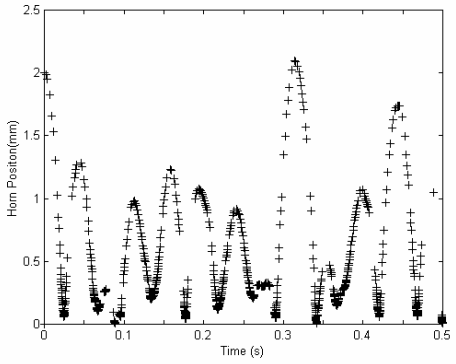

(a) A typical simulation results

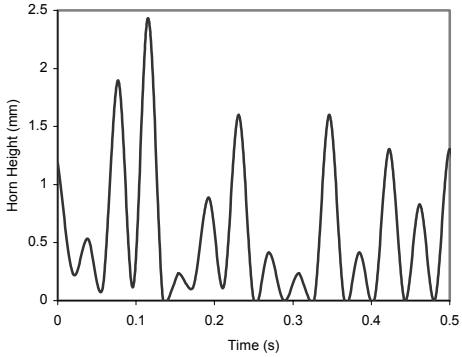

(b) Typical experimental observation

Fig. 18. The body movement of the horn transducer

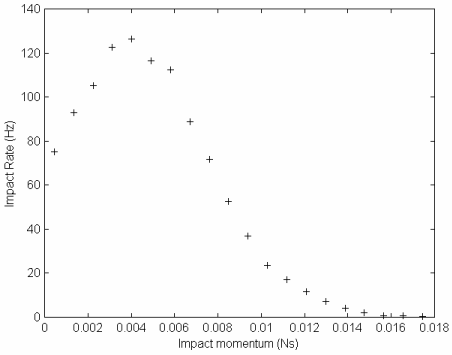

Fig. 19. The impact frequency versus momentum

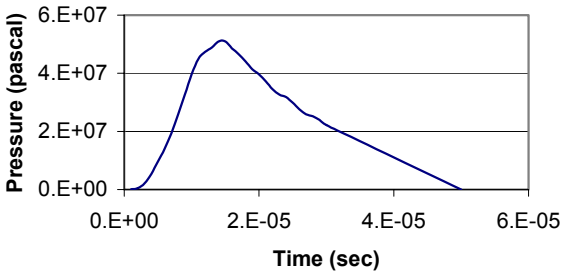

Fig. 20. The figures shows impact loading of the drill by the rock as a function of the time.

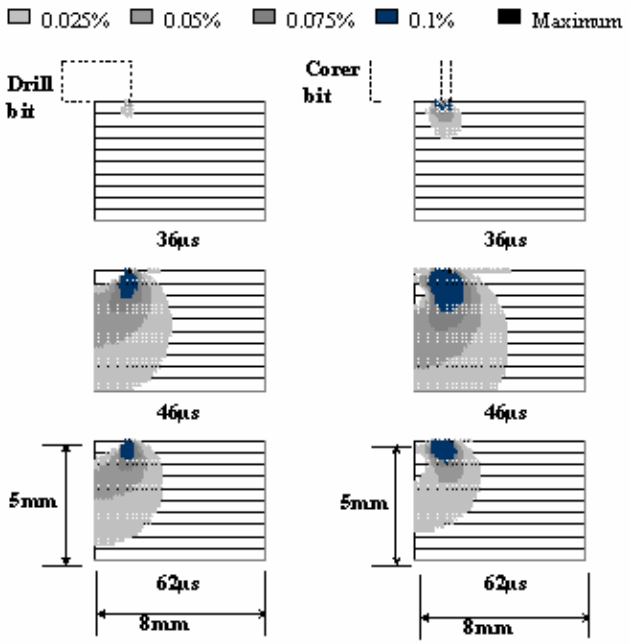

Fig. 21. The principal strain profile at various times after impact of the free-mass on the drill stem for a drilling bit and a coring bit.

H. Estimation of drilling rate

In order to break rock by mechanically induced stresses, sufficient force or energy must be applied to the rock in order induce stresses that exceed the rock's strength. Once this threshold value of force or energy is exceeded, the amount of energy required to break or remove a unit volume of rock remains nearly constant [7]. This energy parameter, which is a measure of the efficiency of the drill, is defined as *specific energy* [8]. The rate at which rock can be crushed, R, equals

$$R = P/E \qquad (33)$$

where P = power input to the rock, joules/sec;

E = specific energy, joules/ cm^3 .

The specific energy E and the compression strength of various types of rocks are listed in Table 2 below [8]

Table 2. Specific energy and compression strength of rocks

Rock type	Compression strength (MPa)	Specific energy (joules/cm^3)
Soft	< 50	30
Medium	50 – 100	50
Hard	100 – 200	260
Very hard	> 200	390

To estimate the drilling rate, we need to know how much energy is transferred from the drill bit to the rock while the stress is higher than the strength of the rock. By using the finite element model mentioned in the previous section, we can construct the force-displacement curve for the surface of rock under the drill bit. A typical force-displacement curve is shown in Fig. 22. The area enclosed by the curve is the total work done to the rock by the drill bit. However, not all the energy transferred to the rock is used to crush the rock. Only the part of the energy that is transferred while the stress is higher than the strength of rock is considered as contributing to rock crushing. The four straight lines in Fig. 23 represent the strength of four different types of rocks, respectively. They are derived from the comparison of the compression strength listed in Table 2, and the force-stresses relationship from the finite element model. To obtain the drilling rate in terms of cm^3 per impact, we would calculate the released energy for the four different values of strength for different types of rocks and divide these values by their respective specific energy. The energy used to crush the rock was approximated by the area limited by the Displacement-Force curve (Fig. 22) that lies above the minimum force lines for a given rock strength.

It should be noted that the force-displacement curve shown in Fig. 22 is derived under the assumption that the loading does not exceed the strength of the rock. Otherwise the curve beyond the strength will appear totally different. However, we have assumed that the energy transferred to the rock is approximately the same.

A statistical analysis of the impact loading in terms of impact momentum vs. frequency is derived from the integrated horn – free-mass – drill-bit model (see Fig.19 for typical momentum transfer distribution). Combining the result shown in Fig. 23 and the calculated energy transferred to the rock at different level of impact momentum, we derive the power used to crush the rock. The drilling rate was estimated by dividing this value by the specific energy (33).

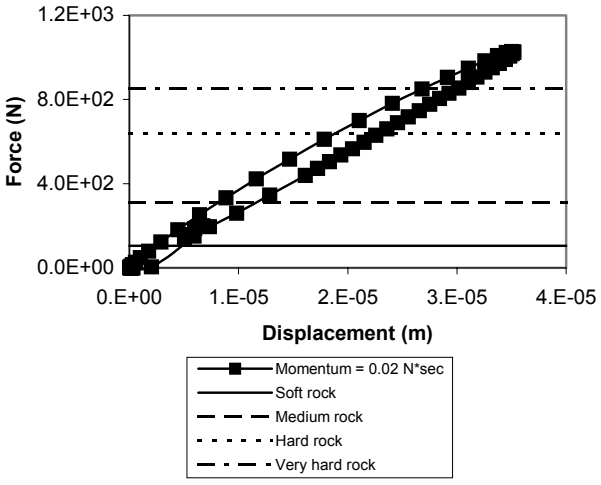

Fig. 22. Force-displacement curve of rock surface under the drill bit.

III. Investigation of Design Parameters and Comparison with Experiments

The model was utilized to investigate and optimize the design of the USDC. One of key design parameters is the mass of the free-mass that transfers energy from the horn to the drill stem. The change of the mass determines the optimum preload of the horn transducer, the energy obtained from the horn and the impact momentum transfer, etc. Figure 23 shows the simulation performance of the drill for different free-mass. We derived the drilling rates of different free-masses for three types of rocks. It is found that, for soft and medium rocks, the drilling rate reaches maximum at a free-mass of about 2 grams. However, for hard rock the 4-gram free-mass predicts a higher drilling rate. These predictions agreed exceedingly well with the experimental findings.

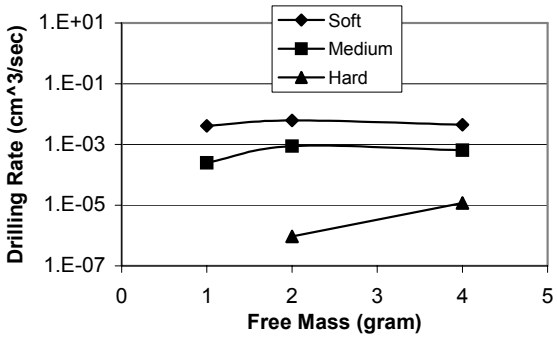

Fig. 23. Drilling rate for different free-masses.

Preliminary studies and experimental tests have shown that the drilling rate increases non-linearly with the input power. Therefore for a given average power, it makes sense to increase the peak input power by using duty-cycle loading. The curves in Fig. 24 show simulated drilling rate for different combinations of peak power and duty-cycle. The average power is maintained at 10 watts by changing the duty cycle appropriately. It is found that the drilling rate increases with the peak power until it reaches a plateau.

Drilling tests were performed on a series of rock samples. These rock samples were suggested by NASA geologists to have similar mechanical properties as expected for the rock types found on Mars. The drilling depth as a function of time is shown in Fig. 25 for a drill bit 2.85 mm in diameter. The test results were performed using 12-Watts average power (24-Watts peak power- 50% duty cycle). The power was measured at the input of the electronics and includes circuit loss of the driving electronics. The efficiency of the electronics was around 70%.

The drilling rate is seen to decrease as a function of the time (depth). It is likely due to a combination of causes including the collection of rock powdered cuttings at the face of the bit damping the impact on the rock, the drag of the tailings on the drill stem and possibly inhomogeneity of the elastic properties of the rock as a function of depth.

There are no hard or very hard rocks such as quartz, corundum or diamond in these rock samples. Most samples belong to rocks of medium hardness. The initial drilling rates for most rocks samples ranged from 1-5x10^{-4} cm^3/s except two samples of Porphyritic Hypersthene Andesile and Basalt Scoria. These two are very porous and fragile than the others in the sample set. The drilling rates for these were determined to be 7.1 and 10x10^{-3} cm^3/s respectively. We divided these rock samples into two groups of medium and soft accordingly. The experimental drilling rates are marked in Fig. 24 for comparison with the simulation and show a general agreement with the model prediction.

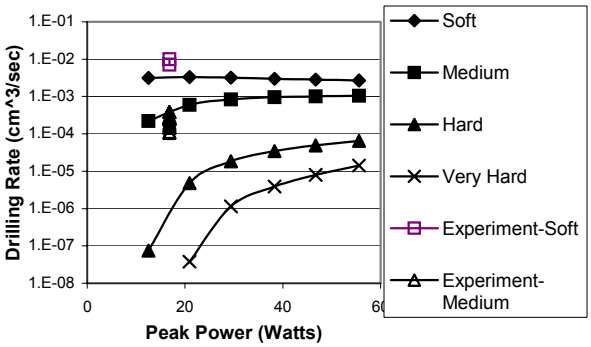

Fig. 24. The curves show the simulated drilling rates as a function of the peak power and the hollow squares and triangles indicate the experimental results. The drill bit is 3 mm in diameter in the simulation and 2.85 mm in the experiment. The category of Experiment-soft includes the samples of Porphyritic Hypersthene Andesite and Basalt Scoria, and the Experiment-medium includes the other rock samples as noted in Fig. 25.

The USDC was modeled to predict its behavior towards the goal of optimizing its performance in various configurations. Physical models were developed for each section of the device and their interactions. The piezoelectric horn transducer was modeled using finite element models and with some simplifications converted to an equivalent circuit to simplify the interaction of the free-mass and electronic driver. The horn tip free-mass interaction was analyzed by a simple collision theory to explore the basic drive mechanism and by finite element approach for accuracy. A spring-mass model was developed to obtain time efficient solutions. Finite element models were also applied to the free-mass/drill bit and the drill bit/rock interactions. The program simulating the operation of the device was integrated from the models of the various parts and their interactions.

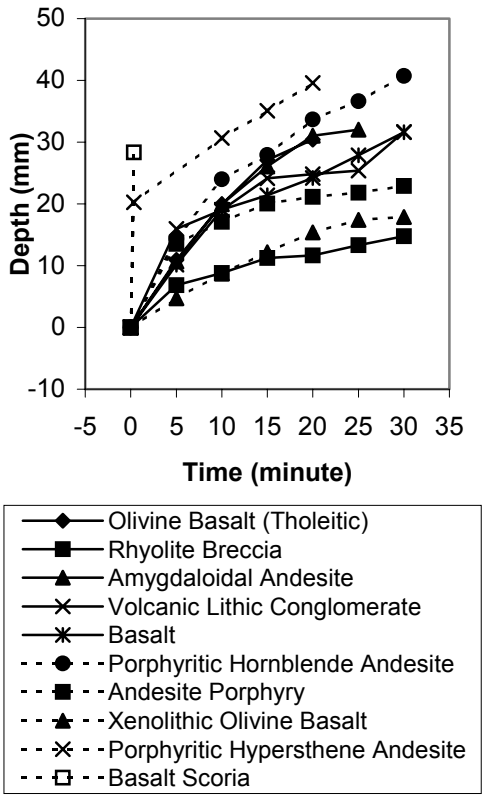

Fig. 25 – The experimental data of drilling depth as a function of time for various rock types.

IV. Conclusions

The developed models allowed for the investigation of the various interactions of the USDC. It was shown that, by using the free-mass, the continuous high frequency vibration of the horn could be converted to low frequency high mechanical power impacts. These impacts created large enough strain in the rock to enable efficient drilling. Using a simulation of the operation of the USDC the characteristics of the USDC performance were investigated and has been used to guide the design of a prototype device. The drilling rates calculated from the model were found to be in agreement with drilling rate data measured on a variety of rock samples.

References

[1] Y. Bar-Cohen, S. Sherrit, B. Dolgin, X. Bao, Z. Chang, R. Krahe, J. Kroh, D. Pal, S. Du, T. Peterson "Ultrasonic/Sonic Driller/Corer (USDC) for planerary application," *Proc. SPIE Smart Structure and Materials 2001*, Volume 4327-55, 2001.

[2] S. Sherrit, X. Bao, Z. Chang, B. Dolgin, Y. Bar-Cohen, D. Pal, J. Kroh, T. Peterson "Modeling of the ultrasonic/sonic driller/corer: USDC," *2000 IEEE Int. Ultrason. Symp. Proc.*, 2000, vol.1,pp. 691-694.

[3] S. Sherrit, B. Dolgin, Y. Bar-Cohen, D. Pal, J. Kroh, T. Peterson, " Modeling of horns for sonic/ultrasonic applications," *1999 IEEE Int. Ultrason. Symp. Proc.*, 1999, pp. 647-651.

[4] H. Allik and T.J.R. Hughes, "Finite Element Method for Piezoelectric Vibration," *Int. J. Num. Math. Eng.*, Vol. 2, 1970, pp. 151-157.

[5] Ansys, *Elements Reference* Release 5.4, Canonsburg, PA: Ansys Inc, 1998, pp. 4-67.

[6] X. Bao, Q. Xu, D. Wang, "Vibration and acoustic radiation of piezoelectric transducers: FEM-equivalent circuit," *Sientia Sinica, Series A: Math., Phys., Astron. Tech. Scie.*, vol. 26, pp. 1285-1294, 1983.

[7] R. Teale, "The concept of specific energy in rock drilling," *Int. J. Rock Mech. Min. Sci*., vol. 2, pp. 57, 1965.

[8] W. Maurer, Novel Drilling Techniques, Pergamon Press, 1968.